Ordered Mesostructured Rare-Earth Fluoride Nanowire Arrays with Upconversion Fluorescence

Fan Zhang,[†] Ying Wan,[‡] Yifeng Shi,[†] Bo Tu,[†] and Dongyuan Zhao*,[†]

Department of Chemistry, Shanghai Key Laboratory of Molecular Catalysis and Innovative Materials, and Laboratory of Advanced Materials, Fudan University, Shanghai 200433, People's Republic of China, and Department of Chemistry, Shanghai Normal University, Shanghai 200234, People's Republic of China

Received February 19, 2008. Revised Manuscript Received April 5, 2008

Ordered mesostructured LaF_3 nanoarrays have been, for the first time, synthesized via a one-step nanocasting process using $La(CF_3COO)_3$ as a precursor and mesoporous silica as a hard template. The characterization of SAXS and XRD patterns and TEM and SEM images shows that the LaF_3 nanowire arrays have long-range regularity of hexagonal mesostructure (*p6mm*) and single-crystalline feature. N_2-sorption isotherms reveal that ordered mesoporous LaF_3 products have high BET specific surface area ($\sim$75 m^2/g), large pore volume (0.15 cm^3/g), and narrow pore-size distribution (the mean value of 4.3 nm). The upconversion fluorescence has been realized in the Yb^{3+}/Er^{3+} (red/green) and Yb^{3+}/Tm^{3+} (blue) codoped LaF_3 nanoarrays by upconversion (UC) excitation in the near-infrared region. The UC emission population for $^4F_{9/2}$, $^2H_{11/2}$, $^4S_{3/2}$, and $^2H_{9/2}$ levels in the Yb^{3+}/Er^{3+} codoped LaF_3 nanowire array matrixes depends on Er^{3+} concentration, the excitation density, and the specific surface areas.

Introduction

Fabrication of patterned and aligned nanostructures in low dimension has huge promise in optoelectronics, lasers, electronics, and biomedical sensors.[1] As for the low-dimensional luminescence materials, significant efforts have been made on semiconductor nanostructures with wide band gap.[1–7] Most recently, upconversion (UC)[8] luminescent materials with unique antistokes optical property have attracted much attention. Colloidal nanocrystals of upconversion rare-earth fluorides doped with lanthanides have been synthesized through the sol−gel process, coprecipitation, and organometallic approaches.[9] To date, no report has demonstrated the fabrication of low-dimensional UC mesostructured nanowire arrays, which are expected for optoelectronic applications.

Nanocasting is one of the most efficient strategies for the fabrication of ordered mesostructured nanowire arrays by using mesoporous silicas as hard templates.[10,11] Despite of the reported various compositions, including carbon, metal and metal oxide replicas,[12] mesostructured metal fluoride nanowire arrays have not been synthesized by the nanocasting strategy yet. The fundamental problem may be the choice of precursor and auxiliary agent.[11] Most of established synthetic methods for metal fluorides are substantially based on the liquid precipitation reaction between soluble metal salts and alkali fluorides. However, the reactions are unsuitable for the nanocasting method since fluorine ions could erode the silica templates. Rare-earth trifluoroacetate complex precursors such as $La(CF_3COO)_3$ have both metal and fluorine elements, and can thermally decompose to LaF_3.[13] This process is interestingly without any erosion of the mesoporous silica SBA-15 templates.

Here we demonstrate the first nanocasting synthesis of ordered mesoporous LaF_3 and lanthanide-doped LaF_3 nanowire arrays with the two-dimensional (2-D) symmetry (space

* To whom correspondence should be addressed. E-mail: dyzhao@fudan.edu.cn
[†] Fudan University.
[‡] Shanghai Normal University.

(1) Wang, X. D.; Song, J. H.; Wang, Z. L. *J. Mater. Chem.* **2007**, *17*, 711.
(2) Huang, M. H.; Mao, S.; Feick, H.; Yan, H. Q.; Wu, Y. Y.; Kind, H.; Weber, E.; Russo, R.; Yang, P. D. *Science* **2001**, *292*, 1897.
(3) Rumbles, G. *Nature* **2001**, *409*, 572.
(4) Xia, Y. N.; Yang, P. D.; Sun, Y. G.; Wu, Y. Y.; Mayers, B.; Gates, B.; Yin, Y. D.; Kim, F.; Yan, H. Q. *Adv. Mater.* **2003**, *15*, 353.
(5) Vayssieres, L. *Adv. Mater.* **2003**, *15*, 464.
(6) Law, M.; Greene, L. E.; Johnson, J.; Saykally, C. R.; Yang, P. D. *Nat. Mater.* **2005**, *4*, 455.
(7) Giesber, H.; Ballato, J.; Chumanov, G.; Kolis, J.; Dejneka, M. J. *Appl. Phys.* **2003**, *93*, 8987.
(8) Downing, E.; Hesselink, L.; Ralston, J.; Macfarlane, R. A. *Science* **1996**, *273*, 1185.
(9) (a) Zhang, F.; Wan, Y.; Yu, T.; Zhang, F. Q.; Shi, Y. F.; Xie, S. H.; Li, Y. G.; Xu, L.; Tu, B.; Zhao, D. Y. *Angew. Chem., Int. Ed.* **2007**, *46*, 7976. (b) Wang, X.; Zhuang, J.; Peng, Q.; Li, Y. D. *Nature* **2005**, *437*, 121. (c) Yi, G. S.; Lu, H. C.; Zhao, S. Y.; Yue, G.; Yang, W. J. *Nano Lett.* **2004**, *4*, 2191. (d) Heer, S.; Kompe, K.; Gudel, H. U.; Haase, M. *Adv. Mater.* **2004**, *16*, 2102. (e) Mai, H. X.; Zhang, Y. W.; Si, R.; Yan, Z. G.; Yan, C. H. *J. Am. Chem. Soc.* **2006**, *128*, 6426. (f) Boyer, J. C.; Vetrone, F.; Cuccia, L. A.; Capobianco, J. A. *J. Am. Chem. Soc.* **2006**, *128*, 7444.
(10) Lu, A. H.; Schüth, F. *Adv. Mater.* **2006**, *18*, 1793.
(11) Wan, Y.; Yang, H. F.; Zhao, D. Y. *Acc. Chem. Res.* **2006**, *39*, 423.
(12) (a) Yang, H. F.; Shi, Q. H.; Tian, B. Z.; Lu, Q. Y.; Gao, F.; Xie, S. H.; Fan, J.; Yu, C. Z.; Tu, B.; Zhao, D. Y. *J. Am. Chem. Soc.* **2003**, *125*, 4724. (b) Tian, B. Z.; Liu, X. Y.; Yang, H. F.; Xie, S. H.; Yu, C. Z.; Tu, B.; Zhao, D. Y. *Adv. Mater.* **2006**, *18*, 1793. (c) Jiao, K.; Zhang, B.; Yue, B.; Ren, Y.; Liu, S. X.; Yan, S. R.; Dickinson, C.; Zhou, W. Z.; He, H. Y. *Chem. Commun.* **2005**, 5618. (d) Joo, S. H.; Choi, S. J.; Oh, I.; Kwak, J.; Liu, Z.; Terasaki, O. *J. Am. Chem. Soc.* **2001**, *123*, 1246.
(13) (a) Lee, J.; Kim, J.; Hyeon, T. *Adv. Mater.* **2006**, *18*, 2073. (b) Lee, J.; Han, S.; Hyeon, T. *J. Mater. Chem.* **2004**, *14*, 478.
(14) (a) Roberts, J. E. *J. Am. Chem. Soc.* **1961**, *83*, 1087. (b) Zhang, Y. W.; Sun, X.; Si, R.; You, L. P.; Yan, C. H. *J. Am. Chem. Soc.* **2006**, *127*, 3260. (c) Sudarsan, V.; Frank, C.; van Veggel, J. M.; Herring, R. A.; Raudsepp, M. *J. Mater. Chem.* **2005**, *15*, 1332.

10.1021/cm800489e CCC: $40.75
Published on Web 05/15/2008

group of *p6mm*) by using $La(CF_3COO)_3$ as precursors.[13] Ordered mesostructured LaF_3 replicas have high BET specific surface areas (up to 75 m^2/g), large pore volumes (0.15 cm^3/g), and uniform pore sizes (the mean value of 3.3 nm). Upon UC excitation in the near-infrared (NIR) region, Yb^{3+}/Er^{3+} and Yb^{3+}/Tm^{3+} codoped LaF_3 nanoarrays display the UC fluorescence. The UC emission including the population of $^4F_{9/2}$, $^2H_{11/2}$, $^4S_{3/2}$, and $^2H_{9/2}$ levels depends on the excitation density, the Er^{3+} concentration and the specific surface areas of the nanowire arrays.

Experimental Section

Preparation of Mesostructured Nanoarrays. Rare-earth trifluoroacetate precursors [$La(CF_3COO)_3$, $Yb(CF_3COO)_3$, $Er(CF_3COO)_3$, and $Tm(CF_3COO)_3$] were prepared according to ref 14. The typical procedure was as follows: 0.24 g (0.56 mmol) of $La(CH_3COO)_3 \cdot 6H_2O$ was added in slight excess to 0.2 g (1.75 mmol) of CF_3COOH. The reaction occurred immediately with evolution of heating to 60 °C for 3 h. Dehydration in vacuum followed by rehydration in a hydrostat over deliquescent sodium bromide yielded pure $La(CF_3COO)_3$. The yield was about 93% on the basis of the $La(CF_3COO)_3$ precursor. The products were analyzed by the precipitation of the rare earth as oxalate and ignition to oxide. Mesoporous silica SBA-15 hard templates were prepared under hydrothermal conditions of 130 °C for 24 h, according to the established procedures.[15] The nonporous silica product was prepared according to the above procedure for SBA-15 without the addition of triblock copolymer P123.

Ordered mesoporous LaF_3 nanoarrays were fabricated by a one-step nanocasting method. In a typical synthesis, 0.27 g (0.56 mmol) of $La(CF_3COO)_3$ was dissolved in 5.0 g (109 mmol) of ethanol with stirring to get a transparent solution. To it 0.15 g of dry SBA-15 hard template was added. After the evaporation of ethanol solvent, the solid product was heated to 300 °C with a rate of 1 °C/min and maintained for 3 h under nitrogen. The silica hard template was then removed by 10 wt % HF solution. The final yield was 95%, calculated on the basis of $La(CF_3COO)_3$. Mesoporous codoped LaF_3 replicas were prepared similarly to the procedure mentioned above. When the precursor solution containing 0.23 g (0.48 mmol) of $La(CF_3COO)_3$, 0.03 g (0.06 mmol) of $Yb(CF_3COO)_3$, and 0.01 g (0.02 mmol) of $Er(CF_3COO)_3$ was used, the mesoporous codoped LaF_3: 10 wt % Yb^{3+}, 2 wt % Er^{3+} nanoarrays were obtained. The preparation of bulk LaF_3: 10 wt % Yb^{3+}, 2 wt % Er^{3+} sample was similar to that of the mesoporous LaF_3: 10 wt % Yb^{3+}, 2 wt % Er^{3+} nanoarrays in the absence of the SBA-15 template.

The mesostructured LaF_3: 10 wt % Yb^{3+}, 2 wt % Er^{3+} nanoarrays with different specific surface areas (the samples were denoted as M1, M2, and M3) were prepared according to the above method with different amounts of SBA-15 templates. The amounts of SBA-15 templates used for the M1, M2, and M3 were 0.4, 0.25, and 0.15 g, respectively.

Characterization and Measurements. Small-angle X-ray scattering (SAXS) measurements were taken on a Nanostar U small-angle X-ray scattering system (Bruker) using Cu Kα radiation (40 kV, 35 mA). The *d*-spacing values were calculated by the formula $d = 2\pi/q$, and the unit cell parameters were calculated from the formula $a = 2d_{10}/\sqrt{3}$. X-ray diffraction (XRD) patterns were recorded on a Bruker D4 X-ray diffractometer with Ni-filtered Cu Kα radiation (40 kV, 40 mA). Nitrogen adsorption−desorption isotherms were measured on a Micromeritics Tristars 3000 analyzer at 77 K. Before the measurements, the samples were outgassed at 180 °C for 6 h in vacuum. The Brunauer−Emmett−Teller (BET) method was utilized to calculate the specific surface area by using adsorption data in the range of the relative pressures (p/p_0) from 0.02 to 0.20. The pore-size distributions (PSD) were derived from the adsorption and desorption branches of the isotherms using the Barrett−Joyner−Halanda (BJH) method, respectively. The total pore volumes, *V*p, were estimated from the amount adsorbed at the relative pressure of $p/p_0 = 0.99$. Transmission electron microscopy (TEM) measurements were conducted on a JEOL 2011 microscope operated at 200 kV. All samples were first dispersed in ethanol and then collected using copper grids covered with carbon films for analysis. Energy-dispersive X-ray (EDX) patterns were performed on a Philips instrument. Scanning electron microscopy (SEM) images were taken with a Philips XL30 electron microscope operating at 20 kV. A thin gold film was sprayed on the sample before the characterization. TG and DTA analyses were carried out on the thermogravimetric analysis TAG 7 and thermal analysis controller TAX 7/DX apparatus (Perkin-Elmer) with a heating rate of 5 °C/min under pure nitrogen flow with a rate of 40 mL/min. Upconversion luminescent spectra were measured on an optical spectrum analyzer (ANDO AQ6317, Japan). The sample was put in a cuvette with 1.0 cm in path length and was excited by a 978 nm CW semiconductor diode laser ($P_{max} = 800$ mW at 1000 mA). The UC luminescence was collected by a multimode optical fiber with the core diameter of 0.6 mm that conducted the luminescence into the optical spectrum analyzer. The distance between the top of the fiber and the sample was about 2 mm. Intensities in the power dependence graphs were calculated based on the integrated area under the peaks of emission spectrum under respective power densities.

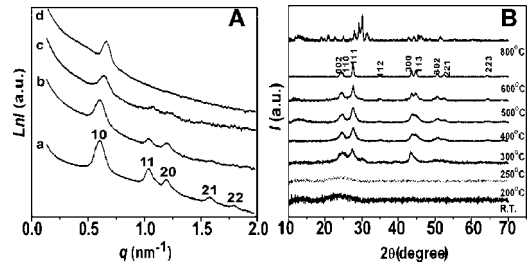

Figure 1. (A) SAXS patterns for the mesoporous silica SBA-15 (a); $La(CF_3COO)_3$/SBA-15 nanocomposites (b); LaF_3/SBA-15 nanocomposites (c) and mesostructured LaF_3 nanoarrays (d). (B) Wide-angle XRD patterns of the $La(CF_3COO)_3$/SBA-15 nanocomposites heated at temperatures ranging from 200 to 800 °C.

Results and Discussion

Ordered mesoporous LaF_3 nanowire arrays were synthesized via a nanocasting route by using mesoporous silica SBA-15 as a hard template and $La(CF_3COO)_3$ as a precursor. SBA-15 templates were prepared at a high hydrothermal temperature of 130 °C. This process can increase the mesotunnels in the pore walls of the mesoporous silica templates. SBA-15 with enhanced mesoporosity of the silica walls has been proven to be beneficial for the production of high-quality replica materials.[12] The SAXS pattern displays well-resolved scattering peaks (Figure 1a), indicating that SBA-15 templates have an ordered 2-D hexagonal mesostructure (space group of *p6mm*) with a cell parameter (a_0) of 10.3 nm. The $La(CF_3COO)_3$/SBA-15 nanocomposites which were cast from the mesoporous silica SBA-15 with

(15) Zhao, D. Y.; Feng, J. L.; Huo, Q. S.; Melosh, N.; Fredrickson, G. H.; Chmelka, B. F.; Stucky, G. D. *Science* **1998**, *279*, 548.

$La(CF_3COO)_3$ precursor display a SAXS pattern (with the same diffraction peak positions) similar to its parents. This result indicates that the mesostructure is stable without the destruction and shrinkage during the nanocasting process. After calcination at 300 °C, three diffraction peaks belonging to the 100, 110, and 200 reflections are retained to some extent with a shift to slightly higher angles. The cell parameter (a_0) is calculated to be 9.5 nm. These phenomena suggest the maintenance of the mesostructure and a slight shrinkage (7.7%) of the domain size upon calcination. The SAXS pattern is less resolved in comparison with the sample before the heating treatment. This can be explained by the reduction of the contrast and X-ray absorption by heavy metal atoms inside the silica nanochannels. The SAXS pattern for the mesoporous LaF_3 product after the elimination of the silica hard template gets less resolved. Only the 100 reflection can be detected, which can be ascribed to the strong X-ray absorption by the heavy metal atoms and some mesostructure defects. The cell parameter (9.5 nm) remains unchanged, indicating that the template-removal process exhibits negligible effects on the domain size. These phenomena demonstrate that mesoporous LaF_3 nanoarrays well replicate the ordered mesostructure of the SBA-15 template.[14,16]

The wide-angle X-ray diffraction (XRD) pattern of the as-made $La(CF_3COO)_3$/SBA-15 nanocomposite (Figure 1B) shows a diffuse diffraction peak, suggesting an amorphous phase. The crystallization does not occur until the temperature reaches 250 °C. The XRD pattern exhibits an obvious change and can be indexed to a hexagonal structure with the lattice parameters of $a = 7.23$ Å and $c = 7.29$ Å (JCPDS 72-1435; $P6_322$) of LaF_3 crystals. This phenomenon, together with the TG result which exhibits a large weight loss at about 250 °C (see below), indicates the thermal decomposition of $La(CF_3COO)_3$ to LaF_3. The diffraction peaks are broad, revealing the nanocrystalline nature of the sample. With the increase of the heating temperature, the diffraction peaks become strong and narrow. This phenomenon is related to the growing size of LaF_3 nanocrystals. Accompanied by the growth of crystals, the mesostructure of the replicas is gradually destroyed if the temperature exceeds 300 °C. The average size of the nanocrystals after calcination at 400 °C is estimated to be 13.2 nm on the basis of the Scherrer formula. The replicated LaF_3 mesostructure increasingly collapses as a result of the crystal size coarsening.[17] A new crystal phase of La_2SiO_5 (JCPDS 40-0234; $P2_1/c$) is yielded when the temperature reaches 800 °C (Figure 1 and Figure S1). The mesostructure simultaneously collapses. Therefore, the thermal decomposition temperature of 300 °C was chosen.[18–21]

The SEM image (Figure 2a) of the ordered mesoporous LaF_3 nanowire arrays, prepared by impregnating $La(CF_3COO)_3$ inside SBA-15 nanochannels after thermally decomposing at 300 °C and removing the silica hard template, exhibits a uniform ropelike morphology. This morphology is similar to its parent SBA-15, suggesting a truthful replication.[12] The size of LaF_3 arrays is about 1.0 μm in length and 0.3−0.5 μm in diameter, a little smaller than that for SBA-15, suggesting a partial filling of mesochannels. $La(CF_3COO)_3$ molecules have strong hydrogen bond interaction with the silanol groups on the surface of SBA-15 templates. This may favor the incorporation of $La(CF_3COO)_3$ into the mesochannels. We further estimated the yield of LaF_3 according to the established model[14] on the basis of the molecular weight and the density of the reagent $La(CF_3COO)_3$ (478 g/mol and 2.25 g/cm^3) and the product LaF_3 (196 g/mol and 5.93 g/cm^3). One cm^3 of $La(CF_3COO)_3$ could produce 0.38 cm^3 of LaF_3. In other words, the theoretical yield is 38 vol %. It is the large filling amount of $La(CF_3COO)_3$ precursor inside mesochannels and the high yield to the LaF_3 product that support the truthful replication of the hard template. The low-magnification TEM image (Figure 2b) reflects the similar phenomena, ropelike morphology, and uniform-size nanowire arrays with the diameter of 1.0−2.0 μm. A long-range regularity can be observed in the whole particle domain. High-magnification TEM images of LaF_3 nanowire products feature ordered hexagonal mesostructures viewed from the [110] (Figure 2c,d) and [001] (Figure 2d inset) directions. These nanowires are uniform in diameter (about 6.0 nm), owing to the confined growth in the channels of the SBA-15 template,[21] and are interconnected by small irregularly distributed metal fluoride rods, as evidenced by the high-resolution TEM (HRTEM) image (Figure 2e). This phenomenon has been demonstrated for mesostructured carbon, metal, and metal oxide replicas.[12]The connections are derived from the micropore around the primary pores of mesoporous silica SBA-15.

The single-crystalline feature is confirmed by the selected-area electron diffraction (SAED) pattern (Figure 2c inset) and HRTEM image (Figure 2e). The *d*-spacing of the single-crystal β-LaF_3 phase is measured to be ~0.38 nm along the [110] direction.[14] The SAED pattern shows some distorted spots, indicating the defects in the single-crystalline products. The EDX spectrum (Figure 2f) reveals that the final product is a pure lanthanum fluoride (LaF_3) phase. No Si is detected. These results suggest a complete removal of the SBA-15 template. The yield is calculated to be about 95 wt % on the basis of the $La(CF_3COO)_3$ precursor.

Figure 3 shows the N_2 adsorption−desorption isotherms of the SBA-15 hard template, LaF_3/SBA-15 nanocomposite, and silica-free mesoporous LaF_3 replicas. The isotherms of SBA-15 template represent typical type-IV curves with an H_1-type hysteresis loop, attributed to perfect cylindrical mesoporous channels. The pore volume is calculated to be 1.12 cm^3/g. The adsorption volume for the LaF_3/SBA-15 composite reduces to 0.52 cm^3/g, implying the loading of LaF_3 in the mesochannels. Mesostructured LaF_3 nanowire arrays after the removal of silica hard template exhibit type-IV isotherms, characteristics of a mesoporous material. Two

(16) Shi, Y. F.; Wan, Y.; Liu, R. L.; Tu, B.; Zhao, D. Y. *J. Am. Chem. Soc.* **2007**, *129*, 9522.
(17) Rumplecker, A.; Kleitz, F.; Salabas, E. L.; Schüth, F. *Chem. Mater.* **2007**, *19*, 485.
(18) Imperor-Clerc, M.; Bazin, D.; Appay, M. D.; Beaunier, P.; Davidson, A. *Chem. Mater.* **2004**, *16*, 1813.
(19) Zhu, K. K.; Yue, B.; Zhou, W. Z.; He, H. Y. *Chem. Commun.* **2003**, 98.
(20) Dickinson, C.; Zhou, W. Z.; Hodgkins, R. P.; Shi, Y. F.; Zhao, D. Y.; He, H. Y. *Chem. Mater.* **2006**, *18*, 3088.
(21) Wang, Y. Q.; Yang, C. M.; Schmidt, W.; Spliethoff, B.; Bill, E.; Schüth, F. *Adv. Mater.* **2005**, *17*, 53.

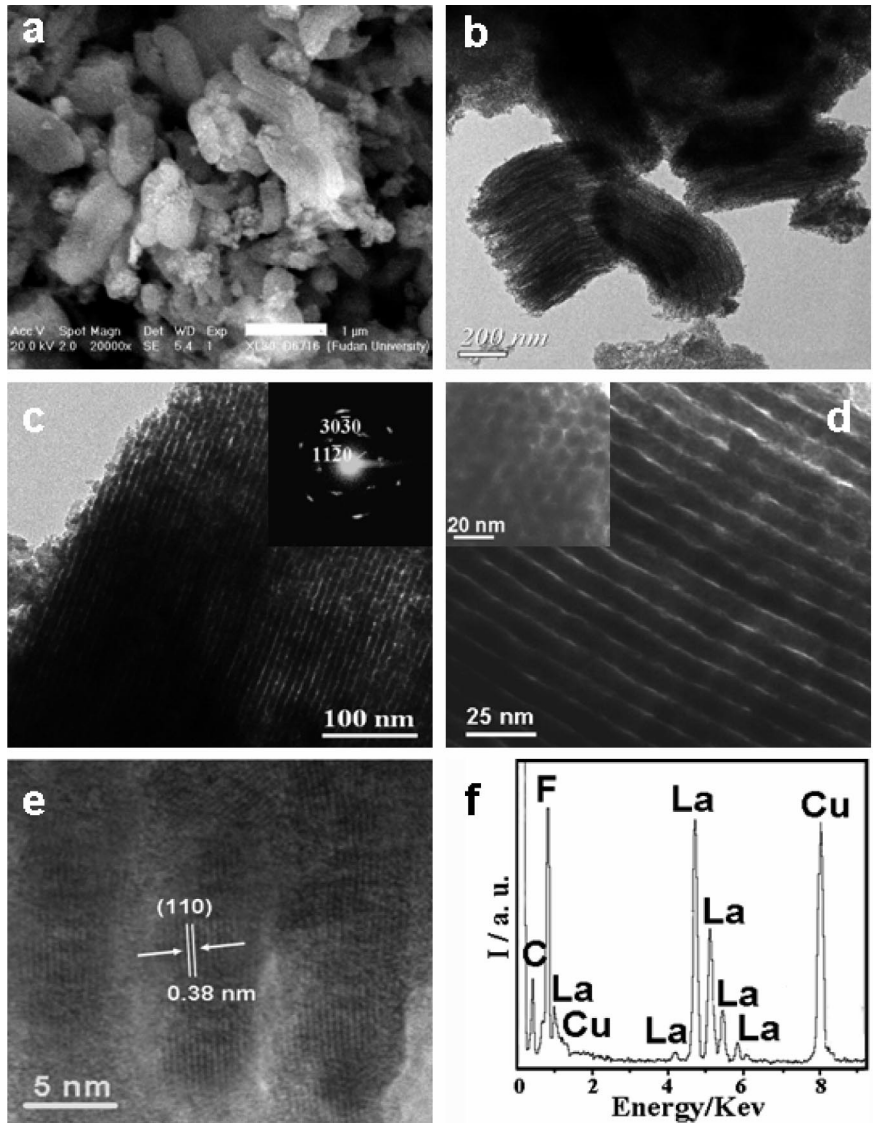

Figure 2. (a) SEM image of the 2-D hexagonally mesostructured LaF_3 with the single-crystalline framework prepared by the nanocasting strategy after the removal of silica hard template. TEM images of ordered mesoporous LaF_3 nanoarrays with the low magnification (b and c) and the high magnification (d) taken along the [110] (b, c, and d) and [001] (inset d) directions. Inset (c) is an SAED image. (e) HRTEM image taken along the [110] direction. (f) EDAX spectrum of mesostructured LaF_3.

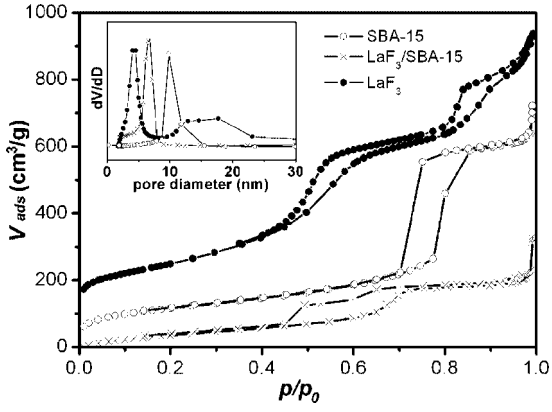

Figure 3. Nitrogen sorption isotherms of the successive products in the synthesis: SBA-15 hard template (O); LaF_3/SBA-15 composites upon calcination at 300 °C (×); and LaF_3 nanoarrays after etching silica by HF solution (•). Inset is corresponding pore-size distribution curves. The adsorption amount of LaF_3 nanoarrays was magnified by 10 times for clarity.

defined steps in the p/p_0 ranges of 0.4−0.6 and 0.8−0.95 are observed. The former step corresponds to the capillary condensation in the main channels templated by SBA-15, confirming the uniform mesopores, while the latter is related to the voids, possibly due to the packing of small particles and the incomplete filling of LaF_3 inside the SBA-15 channels.[22–24] This result can be explained by the partial loading of the $La(CF_3COO)_3$ precursor and the relatively large volume loss from $La(CF_3COO)_3$ to LaF_3.

To elucidate the complete decomposition process of metal fluorides inside the pores of the mesoporous silica, thermal analysis (TG) experiments were performed. The results for pure $La(CF_3COO)_3$ precursor, $La(CF_3COO)_3$/SBA-15 nanocomposite, and $La(CF_3COO)_3$/nonporous silica (prepared similar to the SBA-15 but without the surfactant) are depicted

(22) Tian, B. Z.; Liu, X. Y.; Solovyov, L. A.; Liu, Z.; Yang, H. F.; Zhang, Z. D.; Xie, S. H.; Zhang, F. Q.; Tu, B.; Yu, C. Z.; Terasaki, O.; Zhao, D. Y. *J. Am. Chem. Soc.* **2004**, *126*, 865.
(23) Kim, T. W.; Ryoo, R.; Gierszal, K. P.; Jaroniec, M. L.; Solovyov, A.; Sakamoto, Y.; Terasaki, O. *J. Mater. Chem.* **2005**, *15*, 1560.
(24) Lu, A. H.; Kiefer, A.; Schmidt, W.; Schuth, F. *Chem. Mater.* **2004**, *16*, 100.
(25) Schüth, F. *Angew. Chem., Int. Ed.* **2003**, *42*, 3604.

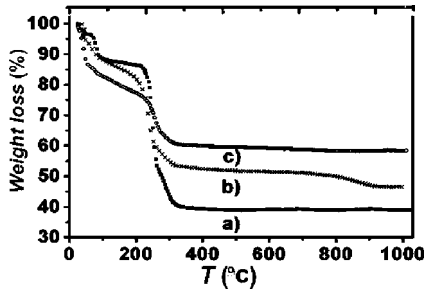

Figure 4. TG curves for pure $La(CF_3COO)_3$ (a); $La(CF_3COO)_3$/SBA-15 nanocomposite (b); and $La(CF_3COO)_3$/nonporous silica (c).

in Figure 4. For pure $La(CF_3COO)_3$, the first weight loss (9 wt %) between 100 and 130 °C is attributed to the release of the crystal water. The second weight loss of 51 wt % in the temperature range from 210 to 290 °C is related to the decomposition of $La(CF_3COO)_3$ to LaF_3. The TG result for the $La(CF_3COO)_3$/SBA-15 nanocomposite reveals the weight loss of 8 and 37 wt % in the same temperature range, respectively. Further increasing the temperature to 700 °C leads to an undetectable weight loss, indicating the almost complete decomposition from $La(CF_3COO)_3$ to LaF_3 at a temperature below 300 °C. An obvious weight loss of 6 wt % occurs between 750 and 860 °C, being ascribed to the formation of La_2SiO_5. The DTA curve of $La(CF_3COO)_3$/SBA-15 nanocomposite shows an obvious exothermal peak (Figure S2), further confirming the formation of La_2SiO_5 phase. The $La(CF_3COO)_3$/nonporous silica composite shows a major weight loss of 15 wt % between 210 and 290 °C, lower than that of the $La(CF_3COO)_3$/SBA-15 nanocomposite. The weight loss above 750 °C disappears, implying the absence of La_2SiO_5. The temperature for the phase transformation to La_2SiO_5 is lower in the $La(CF_3COO)_3$/SBA-15 composite than in the $La(CF_3COO)_3$/nonporous silica, in accordance with the XRD results.

This facile one-step nanocasting route can be extended to the preparation of ordered mesoporous Yb^{3+}/Er^{3+} and Yb^{3+}/Tm^{3+} codoped LaF_3 nanoarrays with 2-D structure by pyrolysis of $La(CF_3COO)_3$ and $Yb(CF_3COO)_3/Er(CF_3COO)_3$ or $Yb(CF_3COO)_3$,/$Tm(CF_3COO)_3$ precursors. The cell parameters, BET surface areas, pore sizes, and pore volumes of the products are listed in Table 1. It clearly shows that the long-range ordered mesostructures of the Yb^{3+}/Er^{3+} and Yb^{3+}/Tm^{3+} codoped LaF_3 nanoarrays (LaF_3: 10 wt % Yb^{3+}, 2 wt % Er^{3+} and LaF_3: 10 wt % Yb^{3+}, 2 wt % Tm^{3+}) are obtained. The codoped process for lanthanides does not cause the obvious effect on the mesostructural regularity. EDX spectrum and elemental analysis (ICP) for the LaF_3: 10 wt % Yb^{3+}, 2.0 wt % Er^{3+} sample (Figure S3) reveal that the content of Yb^{3+} and Er^{3+} is 10 and 2.0 wt %, respectively, which is similar to that in the synthesis batch. It suggests that the final product is Yb^{3+}/Er^{3+} codoped LaF_3. The yields of Yb^{3+}/Er^{3+} and Yb^{3+}/Tm^{3+} codoped LaF_3 nanoarrays are also as high as 93% based on the $La(CF_3COO)_3$ precursor. These results indicate that this nanocasting method is a general route for preparing metal fluoride nanowire arrays. We have also synthesized ordered mesostructured CeF_3, PrF_3, NdF_3, EuF_3, TbF_3, FeF_3, and MnF_2 with high surface areas and narrow pore size distributions (Figure S4, Table S1).

Table 1. Textual Properties of Mesostructured Products[a]

sample name	cell parameter (nm)	BET surface area (m^2/g)	pore size (nm)	pore volume (cm^3/g)
SBA-15	10.3	560	10.2 (8.9)	1.12
LaF_3	9.5	75	4.3 (3.3)	0.15
LaF_3: 10 wt % Yb, 0.2 wt % Er	9.6	69	4.6 (4.6)	0.20
LaF_3: 10 wt % Yb, 0.5 wt % Er	9.4	71	5.0 (4.1)	0.17
LaF_3: 10 wt % Yb, 1.0 wt % Er	9.5	74	4.7 (3.5)	0.15
LaF_3: 10 wt % Yb, 2 wt % Er (M3)	9.2	75	4.9 (3.5)	0.19
M1	9.1	31	9.7 (8.6)	0.11
M2	9.4	61	4.9 (3.6)	0.13
LaF_3: 10 wt % Yb, 2 wt % Tm	9.3	73	4.3 (3.0)	0.21

[a] The pore-size distributions (PSD) were derived from the adsorption and desorption (values in parentheses) branches of the isotherms using the Barrett−Joyner−Halanda (BJH) method, respectively.

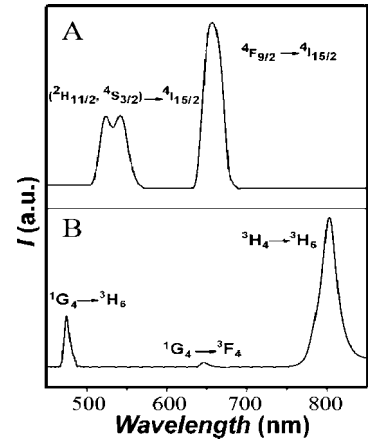

Figure 5. Luminescence emission spectra of mesostructured codoped LaF_3 nanoarrays excited with a 980 nm laser diode at 800 mW: (A) LaF_3: 10 wt % Yb^{3+}, 2 wt % Er^{3+} and (B) LaF_3: 10 wt % Yb^{3+}, 2 wt % Tm.

The UC fluorescence was realized for ordered mesostructured LaF_3 nanowire arrays codoped with Yb^{3+} and Er^{3+} or Yb^{3+} and Tm^{3+} ions (Figure 5). These materials possess structural and textual properties similar to those of the pure mesostructured LaF_3 nanoarrays (Table 1). The visible and NIR upconversion luminescence spectra of LaF_3: 10 wt % Yb^{3+}, 2 wt % Er^{3+} and LaF_3: 10 wt % Yb^{3+}, 2 wt % Tm^{3+} nanorod arrays under infrared excitation at 800 mW (978 nm) (Figure 5) exhibit emission bands assigned to the transitions within 4f−4f levels of Er^{3+} and Tm^{3+} ions.[26–28] In the case of LaF_3: 10 wt % Yb^{3+}, 2 wt % Er^{3+} sample, green luminescence between 520 and 570 nm attributed to the $(^2H_{11/2}, {}^4S_{3/2}) \rightarrow {}^4I_{15/2}$ transition is observed. A dominant red emission is detected in the range of 630−680 nm originating from the $^4F_{9/2} \rightarrow {}^4I_{15/2}$ transition. The signal at around 800 nm, coming from the $I_{9/2} \rightarrow I_{15/2}$ transition in the Er-doped UC material, is not observed in the Yb^{3+}/Er^{3+} codoped LaF_3 nanoarrays.

(26) Stouwdam, J. W.; Frank, C.; van Veggel, J. M. *Nano Lett.* **2002**, *2*, 733.
(27) Sivakumar, S.; Frank, C.; van Veggel, J. M.; Raudsepp, M. *J. Am. Chem. Soc.* **2005**, *127*, 12464.
(28) Sivakumar, S.; Diamente, P. R.; Frank, C.; van Veggel, J. M. *Chem. Eur. J.* **2006**, *12*, 5878.

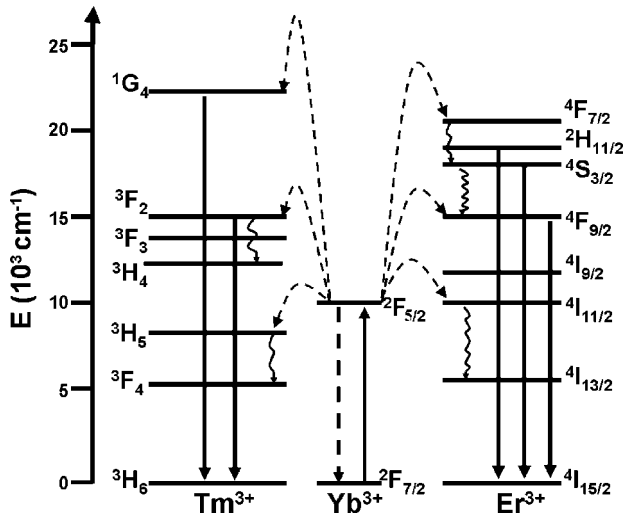

Figure 6. Schematic energy-level diagrams of the Er^{3+}, Tm^{3+}, and Yb^{3+} dopant ions in mesostructured LaF_3: 10 wt % Yb^{3+}, 2 wt % Er^{3+} and LaF_3: 10 wt % Yb^{3+}, 2 wt % Tm^{3+} nanoarrays and the upconversion mechanism excited by a 980 nm laser diode. The solid, dotted, and curly arrows indicate radiative, nonradiative energy transfer, and multiphoton relaxation processes, respectively.

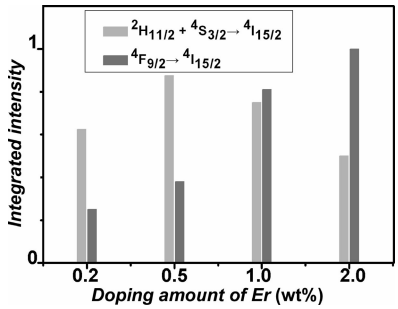

Figure 7. Integrated green ($^2H_{11/2} + {}^4S_{3/2} \rightarrow {}^4I_{15/2}$) and red ($^4F_{9/2} \rightarrow {}^4I_{15/2}$) upconversion emission intensity of the mesostructured LaF_3: LaF_3: 10 wt% Yb^{3+}, 2 wt% Er^{3+} phosphers as a function of Er^{3+} doped levels.

The visible luminescence for LaF_3: 10 wt % Yb^{3+}, 2 wt % Tm^{3+} originates from two stages: $^1G_4 \rightarrow {}^3H_6$ transition results in a blue emission (450−490 nm) and $^1G_4 \rightarrow {}^3F_4$ leads to a weak red emission ranging from 630 to 680 nm. An intense NIR emission is also observed between 750 and 850 nm due to the $^3H_4 \rightarrow {}^3H_6$ transition. The transition mechanism responsible for the UC luminescence is shown in the schematic energy level diagrams (Figure 6).[26–30]

The detailed studies for the UC fluorescence properties of mesostructured materials were performed on Yb^{3+}/Er^{3+} codoped LaF_3 nanoarrays. During the experiment, the raw materials were obtained with very high purities (the purity of the rare-earth materials is above 99.99%) to avoid the impurity effect. When the doping amount of Yb^{3+} (10 wt %) is fixed, the effect of the Er^{3+} content on the UC luminescence properties was investigated. The intensity of the red UC luminescence at 650 nm for the samples with the Er^{3+} content below 1 wt % is always weaker than that of the green emission (Figure 7), similar to the bulk

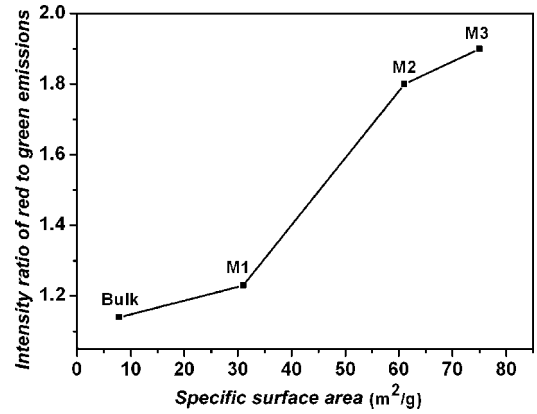

Figure 8. The relationship between the integrated intensity ratio of the green ($^2H_{11/2} + {}^4S_{3/2} \rightarrow {}^4I_{15/2}$) to red ($^4F_{9/2} \rightarrow {}^4I_{15/2}$) upconversion emission and the specific surface area for the codoped LaF_3: 10 wt % Yb, 2 wt % Er phosphers. ("Bulk" denotes bulk materials with the BET specific surface area of 8 m^2/g. M1, M2, and M3 denote the mesostructured nanoarrays with the BET specific surface areas of 31, 61, and 75 m^2/g, respectively).

samples.[31–33] The low nonradiative relaxation rate can explain these phenomena, originating from the wide energy gap between $^4S_{3/2}$ and $^4F_{9/2}$ or $^2H_{11/2}$ and $^4I_{13/2}$ and the low phonon energy in the fluoride matrix. When the Er^{3+} content increases, in the range of 1−2%, the red emission ($^4F_{9/2} \rightarrow {}^4I_{15/2}$) intensity surpasses the green ($^2H_{11/2} + {}^4S_{3/2} \rightarrow {}^4I_{15/2}$) intensity. This should be ascribed to the high nonradiative relaxation rate. According to previous reports,[34] the nonradiative relaxation probability is size-dependent. As the particle size decreases and the specific surface area increases, a number of surface defects with available large vibrational modes such as OH^- (H_2O) are involved, which leads the nonradiative relaxation to become more efficient.

To further clarify this effect, a relationship between the integrated intensity ratio and specific surface areas for the LaF_3: 10 wt % Yb^{3+}, 2 wt % Er^{3+} mesostructured nanoarrays and bulk material was established. As shown in Figure 8, the bulk sample with BET specific surface area of about 7.8 m^2/g and mesostructured nanoarrays with BET surface areas of 31 (M1), 61 (M2), and 75 (M3) m^2/g show that the red emission ($^4F_{9/2} \rightarrow {}^4I_{15/2}$) intensity is enhanced with respect to the green (($^2H_{11/2}$, $^4S_{3/2}$) $\rightarrow {}^4I_{15/2}$) emission with the increasing of the specific surface areas. The intensity ratio of red to green emission increases from 1.15 to 1.9 with the increase of the specific surface areas from 7.8 to 75 m^2/g. Furthermore, absorbed water is detected in the samples. TG analyses (Figure S5) reveal that the water contents for the bulk sample and mesostructured nanoarrays M1, M2, and M3 are 2, 3.8, 4.1, and 8.2 wt % respectively. As a result of that, the nonradiative relaxation becomes more efficient with the increase of specific surface areas, due to the absorption water effect. This effect may lead to a great enhancement of the red emission in the mesostructured nanoarrays.

(29) Menyuk, N.; Dwight, K.; Pierce, J. W. *Appl. Phys. Lett.* **1972**, *21*, 159.
(30) Page, R. H.; Schaffers, K. I.; Waide, P. A.; Tassano, J. B.; Payne, S. A. *J. Opt. Soc. Am. B* **1998**, *15*, 996.
(31) Auzel, F. *Chem. Rev.* **2004**, *104*, 139.
(32) Zhang, J. S.; Qin, W. P.; Zhao, D.; Hu, D. G. J.; Zhang, J.; Wang, H. Y.; Cao, C. Y. *J. Lumin.* **2007**, *122*, 506.
(33) Kramer, K. W.; Biner, D.; Frei, G.; Gudel, H. U.; Hehlen, M. P.; Luthi, S. R. *Chem. Mater.* **2004**, *16*, 1244.
(34) Bai, X.; Song, H.; Pan, G.; Lei, Y.; Wang, T.; Ren, X.; Lu, S.; Dong, B.; Dai, Q.; Fan, L. *J. Phys. Chem. C* **2007**, *111*, 13611.

Conclusion

A simple and general nanocasting route is demonstrated for the synthesis of ordered mesoporous single-crystalline rare-earth fluoride nanoarrays with upconversion fluorescence from mesoporous silica hard templates. $La(CF_3COO)_3$ can be used as an efficient precursor with a high yield (38 vol %). A series of LaF_3 and/or doped with rare-earth ions nanoarrays have been synthesized by a truthful replication of SBA-15 mesochannels, which possess ordered 2-D hexagonal mesostructure, high specific surface areas (up to 75 m^2/g), large pore volumes ($\sim$0.15 cm^3/g), and narrow pore-size distributions (at the mean value of $\sim$3.3 nm). The UC fluorescence is realized in the Yb^{3+}/Er^{3+} (red/green) and Yb^{3+}/Tm^{3+} (blue) codoped LaF_3 nanoarrays by the UC excitation in the NIR region. The ordered nanowire arrays with high Er^{3+} concentration exhibit unique UC luminescence properties. The intensity ratio of red to green emission for LaF_3: 10 wt % Yb^{3+}, 2 wt % Er^{3+} increases with the increase of the specific surface areas due to the absorption water effect.

Acknowledgment. This work was supported by the NSF of China (20421303 and 20521140450), the State Key Basic Research Program of the PRC (2006CB932302), the Shanghai Education and Science & Technology Committee (07QH14011, 06DJ14006, and 07SG49), and Shanghai Nanotech Promotion Center (0652nm024).

Supporting Information Available: EDAX spectrum of Yb^{3+}/Er^{3+} codoped LaF_3, SAXS, wide-angle XRD patterns, and physisorption data of CeF_3, PrF_3, NdF_3, EuF_3, TbF_3, and MnF_2, wide-angle XRD patterns of La_2SiO_5 (JCPDS 40-0234; $P2_1/c$), and TG and DTG curves of the $La(CF_3COO)_3$/SBA-15 nanocomposite (PDF). This material is available free of charge via the Internet at http://pubs.acs.org.

CM800489E